Magnetic-flux profiles of high-T_c superconducting granules: Three-dimensional critical-state-model approximation

R. Navarro* and L. J. Campbell
Theoretical Division, Los Alamos National Laboratory, Los Alamos, New Mexico 87545
(Received 24 June 1991)

Magnetic-flux penetration of high-T_c superconducting (HTS) granules in three dimensions is modeled using spheres and spheroids within the critical-state theory. Numerical approximations for the simplest Bean-London model overlap analytic results in the limits of small and full penetration. Examples for flux contours, initial magnetization, and magnetic hysteresis loops are calculated for the complete range of flux penetration. These results are compared with the solutions for slabs and cylinders so far used in the study of HTS materials. The differences in the flux profiles found for oblate spheroids indicate the inaccuracy of using other geometries in the analysis of HTS flakelike grains.

I. INTRODUCTION

Recently, we analyzed the magnetic-flux penetration in high-T_c superconducting (HTS) powders and ceramics for fields lower than H_{c1}.[1,2] This was done within the framework of effective-medium theories properly adapted to study a superconducting sphere (or spheroid) composite. This effort was one step in the description of how the magnetic field wraps around the grains constituting HTS ceramic materials, which will enable the derivation of other magnetic properties such as the average values of the intergranular fields. Indeed, $H<H_{c1}$ is a field range of relatively low interest because $H_{c1}<H<H_{c2}$ in most applications.

Attempts to describe the magnetic properties of HTS materials for $H>H_{c1}$ has renewed interest in models successfully used during the 1960s (Ref. 3–5) to study hard superconductors. In spite of flux creep in HTS, there remains a wide range of temperature and fields in which the flux vortex lattice is sufficiently pinned to allow critical-state models to be used[6–18] with remarkable qualitative success.

Recently, reported implementations of critical-state models deal with (i) different field dependencies[6,8] or a generalization[9] of the critical current $J_c(H)$, (ii) specific shapes to match experimental geometries of bulk samples[10–12] or their anisotropy,[13] (iii) modifications to describe the intergranular medium[14–16] or the inclusions of nonsuperconducting regions inside the grains,[17] and (iv) extensions to include the essential features of the reversible magnetization near T_c.[18] However, such studies used either one-dimensional geometries (cylinders or slabs with parallel field) or geometries which reduce the critical-state equation within the grain volume

$$\nabla\times\mathbf{H}=\pm\mathbf{J}_c(H)\ , \tag{1}$$

to a one-parameter differential equation. Such analyses, using infinite geometries, are unable to describe how the magnetic flux wraps around the grains.[1] Notwithstanding, the solution for an isolated object is applied to the whole material, which greatly simplifies the problem, but hardly describes the finite shapes of HTS grains.

In the limits of strong and weak magnetic fields, (1) may be solved in more than one dimension. Carr[19] has used such results to build up a continuous, macroscopic electromagnetic description of multifilamentary wires with field components both transverse and longitudinal to a twisted bundle of filaments. This leads to expressions for the average magnetic permeability and electric permitivity and conductivity. In this limit Campbell and Evetts[20] also report results for cylinders and spheres.

The difficulties of solving (1) together with the serendipity that many relevant physical phenomena already occur in one dimension, directly or as a limiting case, may explain the scarcity of studies in three dimensions. The solutions of (1) in two dimensions[21–24] for the magnetization and hysteresis losses in composite multifilamentary wires exposed to transverse and rotating fields were a guide for the methods used here.

Bhagwat and Chaddah[25] claim an exact solution of the Bean-London model[3,4] (BLM) for superconducting spheres. As will be shown here, this claim is inaccurate. To fit the data of a HTS single crystal, Krasnov, Larkin, and Ryazanov[26] have more recently extended BLM to three dimensions. They assumed, arbitrarily, an ellipsoidal shape for the shielded volume together with some simple rules to deduce its change with the applied field. The inaccuracy of this will also be discussed below.

Modeling HTS ceramics as weakly coupled, strongly superconducting grains[27] has been widely used for $H<H_{c1}$.[14–16] Indeed, it is for $H>H_{c1}$ that the physical basis for such modeling is emphasized. There, the analysis of powders and ceramics as a composite of superconducting grains in a nonmagnetic matrix[1] seems to be the natural way to understand their magnetic properties. Moreover, the applicability of the ideas underlying effective-medium theories adds further interest to the three-dimensional solution of the problem.

To this end we consider here first the magnetic-field penetration of an isolated sphere using BLM.[3,4] Rotational symmetry reduces the problem to two dimensions, and both analytic results for the full-penetration case and

numerical solutions for arbitrary applied fields are obtained. After that, initial magnetization and hysteresis loops are calculated from the magnetic-flux profiles. Moreover, we generalize the analytic results to prolate and oblate spheroids with fields parallel and perpendicular to the symmetry axis. Also, numerical methods are employed to calculate the penetration for various strengths of parallel magnetic field. For two representative eccentricities the flux profile and magnetic properties are derived and compared with those of spheres, cylinders, and slabs.

II. BEAN-LONDON MODEL FOR SPHERES

For simplicity we focus on the BLM approach, which assumes a field-independent critical-current density J_c. Although BLM is the simplest case, some of its conclusions have general validity and others may be extended to allow the numerical solution of more complex $J_c(H)$ dependencies using iterative procedures similar to the ones performed for flat disks.[28]

A. Exact results

Consider a sphere of radius a in an applied field $\mathbf{H}_a$ pointing in the z direction. The rotational symmetry implies that the current will flow in circles, i.e., $\mathbf{J}_c=\pm J_c\hat{\boldsymbol{\varphi}}$. Moreover, for fields $0<H_a<H^*$ there is a volume (which we will call the core) with zero magnetic field due to shielding by the outside shell of current. By definition H^* is the minimum field for which the core has zero volume.

The core is bounded by a closed surface $r_k(\theta,H_a)$, which has the rotational symmetry of the system and depends on the magnitude H_a and azimuth angle θ. The existence of reflection symmetry through a plane perpendicular to the z axis in the sphere center further reduces the degrees of freedom. Obviously, $r_k(\theta,H_a)=r_k(2\pi+\theta,H_a)$ and r_k may be expanded in a Fourier series of periodicity 2π. Furthermore, as $r_k(\theta,H_a)=r_k(\pi-\theta,H_a)$, the following expansion holds:

$$r_k(\theta,H_a)=\sum_{n=0}^{\infty}\{a_{2n}\cos(2n\theta)+b_{2n+1}\sin[(2n+1)\theta]\}\ . \tag{2}$$

Exact results for $r_k(\theta,H_a)$ may be found for small penetration of the magnetic field.[20] In this limit the field for points outside of the sphere is[1]

$$\mathbf{H}(r)=\left[H_a+\frac{2C_1}{r^3}\right]\cos\theta\hat{\mathbf{r}}+\left[-H_a+\frac{C_1}{r^3}\right]\sin\theta\hat{\boldsymbol{\theta}},\quad r\geq a\ , \tag{3}$$

and the boundary conditions of $\mathbf{B}$ and $\mathbf{H}$ at $r=a$ give

$$\mu H_r|_{r=a}=0,\quad C_1=-a^3H_a/2\ ,$$
$$H_\theta|_{r=a}=J_{s,\varphi},\quad J_{s,\varphi}=-\tfrac{3}{2}H_a\sin\theta\ , \tag{4}$$

where μ is the permeability of the medium surrounding the sphere and $J_{s,\varphi}$ is the only nonzero component of the surface-current density $\mathbf{J}_s$. In (3) and (4) we assumed the absence of surface barriers for magnetic-flux entry or exit, and so the external field H_a acts at the boundary. Otherwise, following Clem,[29] H_a should be replaced by the appropriate entry or exit field at points on the boundary but inside the superconductor. In the following analysis we do not consider such effects, which could be included by introducing a surface-current density.

From (3) and (4) we find that at the surface of the sphere $H_r=0$ and $H_\theta=-\frac{3}{2}H_a\sin\theta$. Thus the flux begins to penetrate at $\theta=\pi/2$ when $h_a>\frac{2}{3}H_{c1}$. Because H_{c1} in many HTS materials is negligible ($H_a\gg H_{c1}$), we take $H_{c1}=0$, which results in flux penetration at every θ.

It is simple to deduce the penetration depth δ of the critical current for small fields[20] because $J_s=J_c\delta$. The core's surface is then

$$r_k(\theta,H_a)=a-\frac{3H_a}{2J_c}\sin\theta\ . \tag{5}$$

For convenience we will hereafter use reduced units, with the radial variable normalized to the radius a of the sphere ($r'=r/a$) and fields in $aJ_c/2\pi$ units ($h=2\pi H/aJ_c$) such that (5) may be written as

$$r_k'(\theta,h_a)=1-\frac{3h_a}{4\pi}\sin\theta\ , \tag{6}$$

where now $0\leq r_k'<+1$. Indeed, this result fits the Fourier-series expansion (2) and permits derivation of the magnetization[20] in reduced units ($M'=2\pi M/aJ_3$),

$$M'=-\tfrac{3}{2}h_a(1-\tfrac{81}{256}h_a)+O(h_a^3)\ , \tag{7}$$

where $O(h^n)$ stands for terms of order h^n and higher.

The limit of full magnetic penetration also permits the derivation of some exact results. It is simple to calculate h^*, the maximum shielding field, because it is the field found at the center of the sphere when a current $\mathbf{J}=-J_c\hat{\boldsymbol{\varphi}}$ flows at all points. Then $r_k'(\theta,h^*)\equiv 0$, and the limits of the volume integral are trivial,

$$\mathbf{h}^*=-\tfrac{1}{2}\int\frac{\mathbf{r}'\times\hat{\boldsymbol{\varphi}}}{r'^3}dv'=-\frac{\pi^2}{2}\hat{\mathbf{k}}\ , \tag{8}$$

where $\mathbf{r}'$ is the position vector of the volume element dv' referred to the center. The derived h^* value agrees with the bounds of Campbell and Evetts,[20] $4\pi/3<h^*<2\pi$.

Furthermore, in the same limit the magnetic moments induced in the sphere, $\mathbf{m}'(m'=2\pi m/aJ_c)$ are easily derived by evaluating

$$\mathbf{m}'=-\frac{\pi}{a}\int(\mathbf{r}'\times\hat{\boldsymbol{\varphi}})dv'\ . \tag{9}$$

The highest value of the magnetization $M'=m'/V$ ($V=$sphere volume) is reached for fields $h\geq h^*$. In this case the current density will be $\mathbf{J}_c=-J_c\hat{\boldsymbol{\varphi}}$ at all the points of the sphere and

$$M'=-3\pi^2/16\ . \tag{10}$$

Note that this value differs from an earlier estimate,[20]

$M'=-\pi/2$, but agrees with the more recent one of Krasnov, Larkin, and Ryazanov.[26]

The difference between the exact results derived here for the core at small fields (6), the maximum shielded field (8) and magnetization at saturation (10), and the values derived by Bhagwat and Chaddah[25] shows that their approach is not exact, as claimed, for the full range of fields.

B. Numerical implementation

For arbitrary fields in the range $0 \le h \le h^*$, there are no analytical solutions of (1), and different approximations have been used. In an analogous case—the BLM solution for superconducting cylinders in a transversal field—Kato[21] assumed *a priori* an ellipsoidal cylindrical shape for the core. With this boundary usual integral procedures of electromagnetism[30] allow derivation of the field at any point. However, numerical methods,[22–24] which are accurate and require no arbitrary assumptions, have revealed the inaccuracy of the approach of Kato, Hanawaka, and Yamafuji. The same procedure in three dimensions has been followed by Krasnow, Larkin, and Ryazanov,[26] assuming an ellipsoidal shape of fixed length along the direction of the applied field. Certainly the exact result for small fields (6) is not an ellipsoid, and as we prove later, this procedure has the same shortcomings as the result of Kato, Hamanaka, and Yamafuji[21] mentioned above. For our particular geometry we use numerical procedures based on Ashkin's ideas[22] and Frankel's procedures.[28]

By definition the critical current inside the core is zero and Maxwell's equations reduce to $\nabla\times\mathbf{h}=0$ and $\nabla\mathbf{h}=0$. In such cases $\mathbf{h}$ may be derived from a scalar potential Φ, $\mathbf{h}=-\nabla\Phi$, such that $\nabla^2\Phi=0$. Using Green's identities over the volume of the core $V_k(h_a)$, we have

$$\int_{V_k}|\nabla\Phi|^2 dv' = \oint_{r_k(\theta,h_a)}(\Phi\nabla\Phi)\cdot d\mathbf{s}' = -2\pi\int_{\theta=0}^{\pi}(\Phi h_n)\rho' dl' ,$$

where $d\mathbf{s}'=\mathbf{n}ds'$ refers to the surface $r_k'(\theta,h_a)$ bounding the core, n denotes the normal component, $\rho'=\rho/a$ is a normalized cylindrical coordinate, and dl' is the length element of the contour defined by the intersection of the surface $r_k'(\theta,h_a)$ and the plane $\varphi=0$. Thus, if the projection of the total field h_n becomes zero on the above line, it is also zero in the volume V_k.

To derive $r_k'(\theta,h_a)$ we employ, following Ashkin,[22] an error function of the type

$$f_{\rm err}=\frac{1}{N}\sum_{1}^{N}[h_n(r_j',\theta_j)+h_{a,n}]^2 , \tag{11}$$

where $h_n(r_j',\theta_j)$ is the field created by the shielding currents evaluated on a discrete set of N points at the core, $r_j'=r_k'(\theta_j,h_a)$, and $h_{a,n}$ is the normal component of the external field. Minimizing the function $f_{\rm err}$ for any field $\mathbf{h}_a$ enables us to determine the shielded volume.

To minimize $f_{\rm err}$ we follow two optimizing procedures. The first takes advantage of the Fourier expansion (2) containing a set of unknown parameters $(a_{2n},b_{2n+1};\ n=0,1,\ldots,)$, which are obtained minimizing $f_{\rm err}$. However, for $H>0.5$ we need many coefficients to describe $r_k'(\theta,h_a)$ and the convergence is poor. The second uses directly a polygon formed by N points r_j',θ_j, which changes until a minimum in $f_{\rm err}$ is reached. To speed up the process we use only the greater component of $\mathbf{h}_a$ (z projection) in the function $f_{\rm err}$.

For any given contour $r_k'(\theta,h_a)$ the z component of the field created by the induced current is[30]

$$h_z(r_j',\theta_j)=F(r_j',\theta_j;\alpha,\beta) , \tag{12}$$

where $\alpha=r_k'(\theta,h_a)$, $\beta=1$, and

$$F(r,\theta;\alpha,\beta)=-\int_0^{\pi}d\theta'\int_{r'=\alpha}^{\beta}r' f_z(r,\theta;r',\theta')dr' , \tag{13}$$

which takes advantage of the rotational symmetry, and where

$$f_z(r,\theta;r',\theta) = R_+^{-1}K(k)+R_+^{-1}R_-^{-2}\times[(r'\sin\theta')^2-(r\sin\theta)^2-(r\cos\theta-r'\cos\theta')^2]E(k) ,$$

$$R_\pm=[(r\sin\theta\pm r'\sin\theta')^2+(r\cos\theta-r'\cos\theta')^2]^{1/2} ,$$

$K(k)$ and $E(k)$ are complete elliptic integrals of the first and second kind, respectively,

$$K(k)=\int_0^{\pi/2}\frac{d\varphi}{(1-k^2\sin^2\varphi)^{1/2}} ,$$

$$E(k)=\int_0^{\pi/2}(1-k^2\sin^2\varphi)^{1/2}d\varphi ,$$

and $k^2=4r'rR_+^{-2}\sin\theta'\sin\theta$.

In the evaluation of (13) we used Gauss quadrature with different orders for the θ' and r' integrals. Moreover, for the elliptic integrals we used polynomial approximations. Because of proximity, errors appear in the integral evaluation when the discrete loops used in the numerical Gauss quadrature formula and the points at the boundary become too close. To minimize such errors the core contour used in the construction of $f_{\rm err}$ was scaled. After different trials a uniform reduction factor 0.9 was chosen.

A grid of N equally spaced θ_j values was used in the polygonal r_j',θ_j allowing free changes in r_j' (<1) to minimize $f_{\rm err}$. Two N values were used, $N=21$ and 41 [which, by symmetry, reduces to $(N+1)/2$ independent parameters], but most results were derived with the lower value. The degree of the Gauss quadrature formula was always high enough ($>N$) to avoid oscillations on the contour. Furthermore, between two adjoining points a linear interpolation was made in the r',θ plane.

In optimizing $f_{\rm err}$ for small applied fields, we used as an initial guess a polygon obtained with the analytic expression (6). For higher fields the polygon obtained in the previous lower field was used as initial trial after being scaled. To avoid (or detect) convergence to a relative minimum of $f_{\rm err}$, several runs with different trial functions were made. For values $\pi/4<\theta<\pi/2$ the r_j' convergence is fast and unambiguous, and for $\theta=\pi/2$ the es-

timated accuracy is better than 1 per 1000. However, for $\theta < \pi/10$ both convergence and accuracy are reduced, being lowest for $\theta=0$, but always better than 1%.

Because we used only the z component of the field in the error function (11), we checked the results by also calculating $h_\rho(r'_j,\theta_j)$ at the core's surface. In the worst case (for very small field), h_ρ remains three orders of magnitude lower than h_z (i.e., within the numerical error $h_\rho=0$). Moreover, both h_z and h_ρ were calculated for points inside the core and showed the same characteristics as at the surface.

C. Characteristics of the core surfaces

The results derived for $r_k(\theta,h_a)$ are depicted in Fig. 1 for different applied fields $0<h_a<h^*$. Up to $h_a\approx 0.75$ the core's apex almost coincides with the sphere's pole and, for higher fields, goes deeply inside the sphere. The shape remains elongated until it disappears at $h_a=h^*$. The results for small fields ($h_a\approx 0.05$) overlap the exact expressions (6) within the estimated error. Furthermore, in the limit of almost full penetration, the calculated shape agrees with the analytic results obtained with a Taylor-series expansion around the origin, which gives $h_z(\rho=0,z)-h_z(0,0)\sim z^2$, whereas $h_z(\rho,z=0)-h_z(0,0)\sim\rho$.

The derivation of other physical magnitudes of interest is greatly facilitated by using two main properties of the $r'_k(\theta,h)$ surfaces.

(i) By construction, if current of the same density and direction $\mathbf{J}=J_c\hat{\boldsymbol{\varphi}}$ flows at all points, $r'_k(\theta,h)\le r'\le 1$, but the current is zero for $r'\le r'_k(\theta,h)$; then inside this core a constant field $\mathbf{h}$ is created parallel to the z axis. For points of the sphere outside the core, $\mathbf{h}$ changes with position, although it has only a z component.

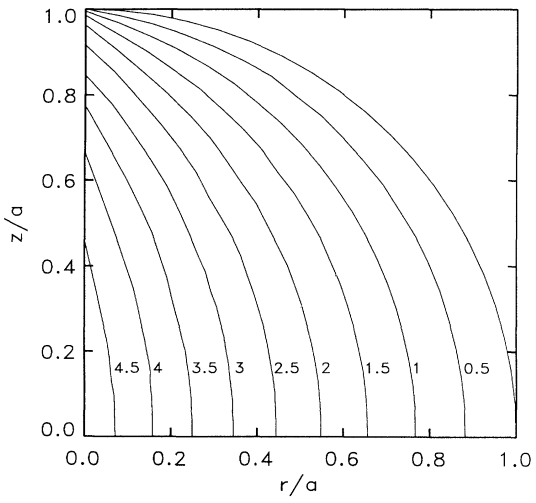

FIG. 1. First quadrant of the magnetically shielded volume (core) for a sphere in different external fields. The curves are labeled with the value of $h=2\pi H/aJ_c$, and the coordinates are scaled to the radius.

(ii) All the surfaces $r'_k(\theta,h)$ for $0<h\le h^*$ have a sharp apex and fill the sphere in a uniform and unique way (i.e., any r',θ corresponds to only one h except for the points $r'=1$, $(\theta=0,\pi)$.

Comparison of these self-consistent solutions of the core shape for spheres with the starting hypothesis of Krasnov, Larkin and Ryazanov[26] reveals the rough approximation of their assumed ellipsoidal core. An important characteristic is common: The field inside the superconductor has only a z component and is uniform at saturation. However, even at small fields, where an analytic solution exits, the shielded volume is *not* ellipsoidal, but exhibits sharp apexes which coincide with the poles only in a limited range of applied fields. This discontinuity at the core surface is possible only at points where the total field is zero.

D. Magnetic shielding

It is simple to derive the z component of the flux profile using the results for $r'_k(\theta,h_a)$. Representing the radial and azimuthal dependencies of the flux profile as $\tilde{h}_z(r',\theta)$, for $h_a<h^*$, the points of the core are such that

$$\tilde{h}_z(r',\theta)=0,\quad r'\le r'_k(\theta,h_a)\ . \tag{14}$$

Outside, the profile is obtained by noting that for the field h_a on the surface $r'_k(\theta,h')$ there is a field $-h'$ created by the outside $[r'\ge r'_k(\theta,h')]$ induced currents and another contribution due to the inside $[r'_k(\theta,h_a)\le r'\le r'_k(\theta,h')]$ ones, which, with the help of (13), is written as

$$\tilde{h}_z(r',\theta)=h_a-h'+F(r',\theta;\, r'_k(h_a),r'_k(h'))\ ,\qquad 0\le h'\le h_a\ . \tag{15}$$

For $h_a>h^*$ there is no core and the flux profile is

$$\tilde{h}_z(r',\theta)=h_a-h'+F(r',\theta;\, 0,r'_k(h'))\ ,\qquad 0\le h'\le h^*\ . \tag{16}$$

The expressions (14)–(16) are valid only for increasing fields. For more complex magnetic histories the derivation of the flux profile follows the same simple principles. In the next section, and as an example, we will consider the case in which, after reaching a value h_0 by monotonic increase, the field is reduced (also continuously) to another value $h_a<h_0$. There are two possibilities.

(i) For $h_0<h^*$ the flux profile created by h_0 remains for points inside a surface $r'_k(\theta,h_p)$, $h_p=(h_0-h_a)/2$. In this way the field remains zero for $r'\le r'_k(\theta,h_0)$, whereas for $r'_k(\theta,h_0)\le r'\le r'_k(\theta,h_p)$ it takes the values

$$\tilde{h}_z(r',\theta)=h_0-h'+F(r',\theta;\, r'_k(h_0),h'_k(h'))\ ,\qquad h_p\le h'\le h_0\ . \tag{17}$$

For points outside $r'_k(\theta,h_p)$ the flux profile is

$$\tilde{h}_z(r',\theta)=h_a+h'+F(r',\theta;\, r'_k(h_0),r'_k(h_p))-F(r',\theta;\, r'_k(h_p),r'_k(h'))\ ,\qquad 0\le h'\le h_p\ . \tag{18}$$

(ii) For $h_0 > h^*$ and $|h_p| < h^*$, (17) and (18) are valid, but with new bounds $h_p \le h' \le h^*$ for (17). However, if $|h_p| > h^*$, then the flux profile will be

$$\tilde{h}_z(r',\theta) = h_a + h' + F(r',\theta; 0, r_k'(h')) , \quad 0 \le h' \le h^* . \tag{19}$$

The complex form of $r_k(\theta,h_a)$ gives a nonlinear penetration that depends on the angle θ, as seen in Fig. 2, where we have depicted the flux profile for an applied field of h^*. This variation differs from that in one-dimensional geometries, which in the BLM gives linear profiles.[3] It should be noted that the field takes different values at the surface of the sphere. For $h_a = h^*$ at $\theta = \pi/2$, $h_z \approx 1.11 h_a$, whereas for $\theta \ge \pi/4$, $h_z < h_a$ at $\theta = 0$, it reaches a minimum value of $h_z \approx 0.577 h_a$. This distribution of field should be compared with the corresponding one for Meissner state (4) for which $h_z = \frac{3}{2} h_a$ at $\theta = \pi/2$ and $h_z = 0$ at $\theta = 0$. From this extreme increasing the field decreases the ratio h_z/h_a at $\theta = \pi/2$ and increases it at $\theta = 0$; it becomes unity at both locations for $h_a \gg h^*$. Thus the core changes in size and shape with the field, thereby precluding any convenient resort to field-independent demagnetizing factors.

E. Magnetization and hysteresis loops

In deriving the magnetization we used the relation for magnetic moments. The initial magnetization is obtained from (9), recognizing that for $r \le r_k(\theta,h_a)$ there is no current. Thus the direct integral for $0 \le h_a \le h^*$ gives

$$M_z'(h_a) = \frac{3\pi}{8} \left[\int_{\theta=0}^{\pi} r_k'^4(\theta,h_a) \sin^2\theta \, d\theta - \frac{\pi}{2} \right] , \tag{20}$$

whereas $M_z' = -3\pi^2/16$ for $h_a > h^*$.

More complex magnetic histories are worked out in the same way. If after reaching a field $h_0 \le h^*$ we decrease it to h_a,

$$M_z'(h_a) = \frac{3\pi}{8} \left[\frac{\pi}{2} - \int_{\theta=0}^{\pi} [2 r_k'^4(\theta,h_p) - r_k'^4(\theta,h_0)] \sin^2\theta \, d\theta \right] . \tag{21}$$

if $h_0 > h^*$, the magnetization should be

$$M_z'(h_a) = \frac{3\pi}{8} \left[\frac{\pi}{2} - \int_{\theta=0}^{\pi} 2 r_k'^4(\theta,h_p) \sin^2\theta \, d\theta \right] . \tag{22}$$

In Fig. 3 we show the initial magnetization and hysteresis loop for three different fields: $h^*/4$, $h^*/2$, and h^*.

III. GENERALIZATION TO OTHER GEOMETRIES

As explained in the Introduction, the numerical method used in the BLM solution takes advantage of the rotational symmetry, reducing the problem of solving (1) to two dimensions. Thus it may be applied to any system with such characteristics. In particular, its implementation for prolate or oblate spheroids is straightforward when the applied field is parallel to the symmetry axis because in these cases there are only components of the field parallel to this axis inside the spheroid. For both cases all the arguments used to derive the Fourier expansions of the core (2) are valid and will be used here.

Using the physical arguments and procedures of Sec. II A, we first derive analytic results for spheroids in both limits of small and full penetration. This will determine the bounds of the problems and be a guide to the numerical procedures.

A. Prolate-spheroid analytic results

Prolate spheroids ($a > b = c$) are characterized by the eccentricity $e = (1 - b^2/a^2)^{1/2}$ with the bounds (spheres) $0 \le e \le 1$ (cylinders). We use the same normalization for

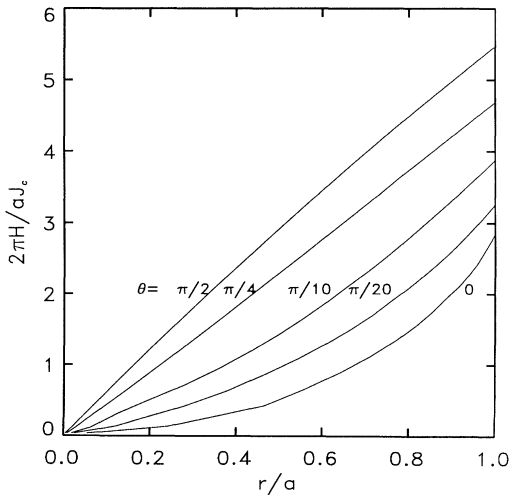

FIG. 2. Flux profile $h_z(r,\theta)$ for different azimuth angles θ and applied field $h^* = 4.9348$.

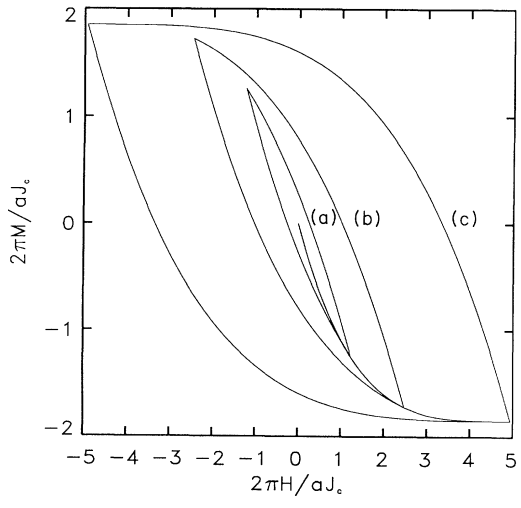

FIG. 3. Initial magnetizations M_z and hysteresis loops for different applied fields (a) $h_{max} = h^*/4$, (b) $h^*/2$, and (c) h^*.

the field and distances as for spheres, but now with the elongated semiaxis distance a.

In the limit of full penetration it is easy to derive the minimum parallel field for which the core's volume becomes zero, because the solution of (8) for spheroids is straightforward, giving

$$h_{\parallel}^{*}=2\pi(1-e^{2})^{1/2}[(1-e^{-2})K(e)+e^{-2}E(e)] , \quad (23)$$

where $K(e)$ and $E(e)$ are elliptic integrals. Indeed, for $e\rightarrow 0$, (23) reproduces the results for spheres, and when $e\rightarrow 1$, the results for cylinders [$h^{*}=2\pi(1-e^{2})^{1/2}$, i.e., $H^{*}=J_c b$]. Moreover, in the same limit the evaluation of (9) gives the magnetization at saturation, reached when $h_a \geq h_{\parallel}^{*}$,

$$M'_{\parallel}=-\frac{3\pi^{2}}{16}(1-e^{2})^{1/2} , \quad (24)$$

which for $e\rightarrow 0$ coincides with the results of (10) and agrees with previous results.[26] However, it should be noted that the derived un-normalized magnetization $M_{\parallel}=3\pi J_c b/32$ or, directly, (24) in the limit $e\rightarrow 1$ gives $M_{\parallel}/H_{\parallel}^{*}=3\pi/32$, whereas the correct result for cylinders is $M_{\parallel}/H_{\parallel}^{*}=\frac{1}{3}$.[14] This discrepancy is due to the fact that the ratio of the maximum magnetization of a finite cylinder of the same radius and length $2a$, $M=J_c b/3$, and that of a prolate spheroid of the same characteristics is $M_{\rm sph}/M_{\rm cyl}=9\pi/32$, which remains constant in the limit $e\rightarrow 1$.

For small penetration the use of prolate-spheroidal coordinates (u,v,φ) following the same steps (3)–(7) enables us to derive the shape of the core for both parallel- and perpendicular-field incidence. These coordinates are related to cylindrical (ρ,z,φ) by[31]

$$\frac{z^{2}}{u^{2}}+\frac{\rho^{2}}{u^{2}-l^{2}}=1, \quad u\geq l; \quad \frac{z^{2}}{v^{2}}-\frac{\rho^{2}}{l^{2}-v^{2}}=1, \quad v\leq l ,$$

where $2l$ is the focal distance of the spheroid. For different u values we obtain a series of confocal prolate spheroids, whereas for constant v values a family of confocal rotational hyperboloids orthogonal to the spheroids is obtained.

Close to the spheroid the magnetic field may be derived from a potential $\Phi(u,v,\varphi)$ such that $\mathbf{H}=-\nabla\Phi$.[31] For parallel incidence this is

$$\Phi=H_a uvl^{-1}-AvQ_1(ul^{-1}) , \quad (25a)$$

whereas, for perpendicular incidence (field pointing in the x axis direction),

$$\Phi=\{-H_a l^{-1}[(u^{2}-l^{2})]^{1/2} - AQ_1^{1}(ul^{-1})\}(l^{2}-v^{2})^{1/2}\cos\varphi , \quad (25b)$$

where $Q_1(z)=(z/2)\ln[(z+1)/(z-1)]-1$ is a Legendre function of the second kind and

$$Q_1^{1}(z)=(z^{2}-1)^{1/2}\{z/(z^{2}-1)-\tfrac{1}{2}\ln[(z+1)/(z-l)]\}$$

is an associated one.

In these coordinates the spheroid is determined by its longest semiaxis $u=a$. Moreover, for small penetration the boundary conditions at the surface are $B_u=\mu H_u=0$, $H_v=-J_{s,\varphi}$, and $H_{\varphi}=J_{s,v}$, with $J_{s,\varphi}$ and $J_{s,v}$ being the components of the surface supercurrent. This implies that the field is maximum at the surface with values of $H_v=H_a/[1-g_{\parallel}(e)]$ in the equatorial plane ($v=0$) for parallel incidence, whereas it is $H_v=H_a/[1-g_{\perp}(e)]$ in the meridian plane ($\varphi=\pi/2$) for the perpendicular ones, where

$$g_{\parallel}(e)=\frac{1-e^{2}}{2e^{3}}\left[\ln\left[\frac{1+e}{1-e}\right]-2e\right]$$

and $g_{\perp}(e)=[1-g_{\parallel}(e)]/2$ are characteristic shape factors,[30,31] which for spheres ($e=0$) reduce to $g_{\perp}(0)=g_{\parallel}(0)=\frac{1}{3}$, and for $e\rightarrow 1$ become $g_{\parallel}(0)=0$ and $g_{\perp}(0)=\frac{1}{2}$.

The penetration depth δ is related to the modulus J_s by $J_s=J_c\delta$. The core's surface is then $u_{k,\beta}=a-\delta/g_{uu}$, where β refers to the parallel or perpendicular orientation of the field and g_{uu} is a metric tensor element:

$$g_{uu}=[(u^{2}-v^{2})/(u^{2}-l^{2})]^{1/2} ,$$

FL evaluated at $u=a$. Using reduced coordinates ($u'=u/a$, $v'=v/a$, with $-e\leq v'\leq e$), the core's surface is

$$u'_{k,\parallel}(v',h_a)=1-\frac{h_a(1-e^{2})^{1/2}}{2\pi e[1-g_{\parallel}(e)]}\frac{(e^{2}-v'^{2})^{1/2}}{1-v'^{2}} , \quad (26a)$$

$$u'_{k,\perp}(v',h_a)=1-\frac{h_a(1-e^{2})^{1/2}}{2\pi e[1-g_{\perp}(e)]} \times\frac{[e^{2}(1-v'^{2}+\cos^{2}\varphi(v'^{2}-e^{2})]^{1/2}}{1-v'^{2}} . \quad (26b)$$

Using the solution for the core, the analytical evaluation of the integral (9) between $u'=u'_{k,\beta}$ and $u'=1$ yields the magnetization for small fields,

$$M'_{\beta}=-\frac{h_a}{1-g_{\beta}(e)}+O(h_a^{2}) . \quad (27)$$

Indeed, (26) and (27) in the $e\rightarrow 0$ limit reproduce the results for spheres [Eqs. (6) and (7)].

B. Prolate spheroid, numerical results

Estimates of the flux penetration for parallel fields in the complete range of fields $0\leq h_a\leq h_{\parallel}^{*}$ are derived using the same numerical procedures described in Sec. II B, and so here we will note only the differences. The determination of the core's shape was made using polygonal r,θ variables, but increasing the number of points ($N=27$–31). However, instead of an equally spaced θ grid, the mesh was adapted to the particular eccentricity. The numerical quadrature procedure was also adapted to follow the grid of the polygon. In all cases the mesh was smallest near $\theta=0$.

The analytic results for the core [Eq. (26a)] were used as an initial guess for the polygon. For small fields $h_a<0.01$, the N-point polygon cannot satisfactorily

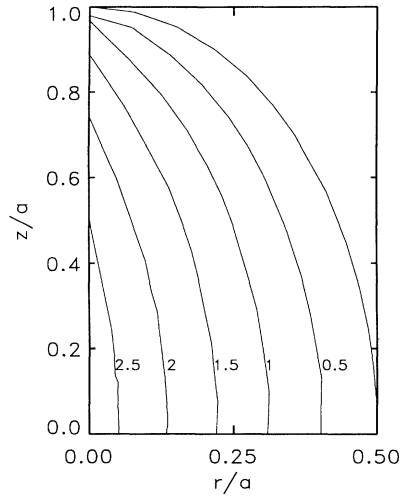

FIG. 4. Contours of the prolate spheroid and magnetically shielded volumes when $a/b=2$ ($h_{\parallel}^{*}=2.814\,56$) for different external fields, $h=2\pi H/aJ_c$, applied in the direction of the symmetry axis. The cylindrical coordinates are scaled to the longest length.

reproduce the core shape except for very high N. Thus, instead of a numerical estimate of the core, we used directly the analytical expression (26a). As in the case of spheres, good agreement between the numerical results and those estimates are found for a range of small fields. To optimize $f_{\rm err}$ for spheroids we used only the simplest downhill-type minimization method.

Figure 4 shows the core's shape for a prolate spheroid with $a/b=2$ ($e=0.866\,03$, $h_{\parallel}^{*}=2.814\,56$). As expected, there are many similarities with the shielding volumes found for spheres: The core shapes are almost the same, and with the correction for the eccentricity, the flux penetration for a given azimuth follows closely the curves of Fig. 2.

Figure 5 shows the same result for a more extreme eccentricity $a/b=10$ ($e=0.994\,987$, $h_{\parallel}^{*}=0.621\,36$). To emphasize the similarities with the lower eccentricity, a $5\times$ expanded scale is used for the horizontal axis. Note, however, that the flux profile at $\pi/2$ is almost linear in h.

Using the core's surface for a given field, the magnetization is derived using (9), taking account that the spheroid surface is now

$$r_s'(\theta)=[(1-e^2)/(1-e^2\cos^2\theta)]^{1/2}\ .$$

For example, the initial magnetization for $0\le h_a\le h_{\parallel}^{*}$, using $V=4\pi a^3(1-e^2)/3$, is given by

$$M_{\parallel}'(h_a)=\frac{3\pi}{8(1-e^2)}\int_{\theta=0}^{\pi}[r_k'^4(\theta,h_a)-r_s'^4(\theta)]\sin^2\theta\,d\theta\ . \tag{28}$$

In Figs. 6 and 7 are shown the initial magnetizations and hysteresis loops for the above two cases. With increasing eccentricity the curves decrease their slopes as well as the values of the magnetization at saturation.

C. Oblate spheroids, analytic results

We apply the same procedures to oblate spheroids ($a=b>c$). First, we derive analytic results in the limiting cases. We use the parameter $e^{*}=(1-c^2a^2)^{1/2}$ such that (spheres) $0\le e^{*}\le 1$ (disks), which is related to the eccentricity by $e'=e^{*}(1-e^{*2})^{-1/2}$. Normalizing to the longest axis a, we obtain

$$h_{\parallel}^{*}=2\pi(e^{*})^{-2}(1-e^{*2})^{1/2}[K(e^{*})-E(e^{*})]\ , \tag{29}$$

which for $e^{*}\to 0$ also reproduces the results for spheres, whereas for $e^{*}\to 1$, $h_{\parallel}^{*}=0$.

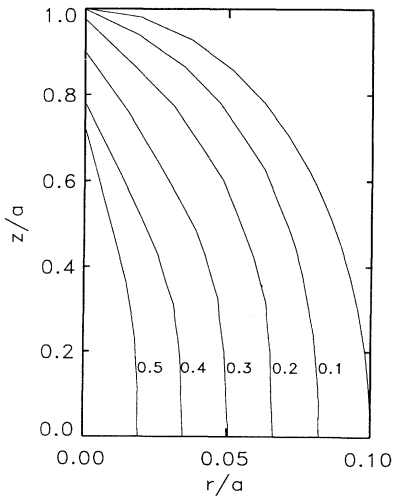

FIG. 5. First quadrant of the magnetically shielded volume for a prolate spheroid when $a/b=10$ ($h_{\parallel}^{*}=0.621\,36$). The same criteria as in Fig. 4 are used.

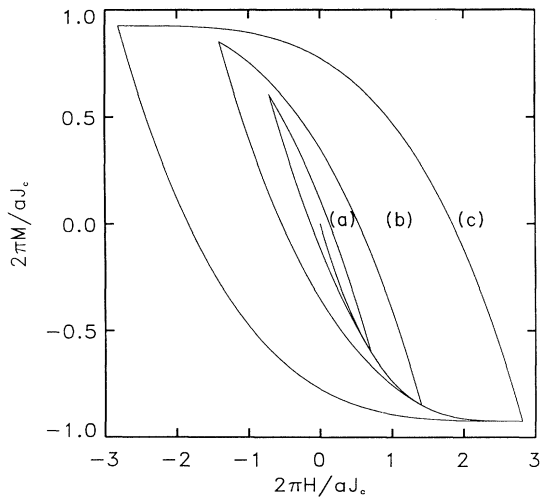

FIG. 6. Initial magnetizations $M_{\parallel}$ and hysteresis loops for a prolate spheroid with $a/b=2$ ($h_{\parallel}^{*}=2.814\,56$) for (a) $h_{\rm max}=h_{\parallel}^{*}/4$, (b) $h_{\parallel}^{*}/2$, and (c) $h_{\parallel}^{*}$.

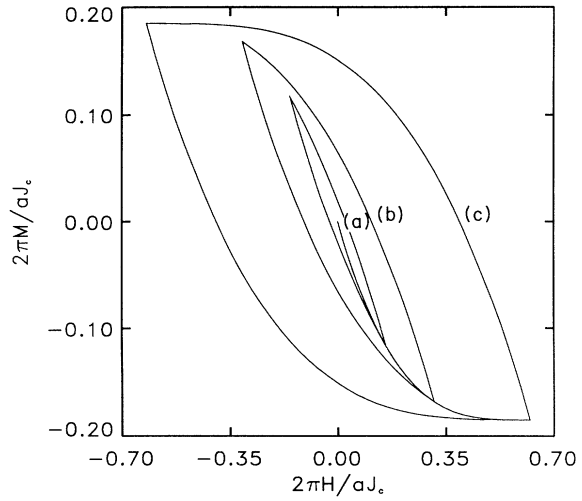

FIG. 7. Initial magnetizations $M_\parallel$ (in $aJ_c/2\pi$ units) and hysteresis loops for a prolate spheroid with $a/b=10$ ($h_\parallel^*=0.621\,36$) for (a) $h_{\max}=h_\parallel^*/4$, (b) $h_\parallel^*/2$, and (c) $h_\parallel^*$.

The value at saturation of $M'_\parallel$, which is obtained when the volume of the core becomes zero, is now equal to (10), independent of the e^* parameter. The same independence from the eccentricity is also obtained for prolate spheroids (24) if the normalization is made to the radius b instead of a.

To obtain predictions in the small-penetration limit, we use here oblate-spheroidal coordinates (u,v,φ),[31] which are related to the cylindrical ones by

$$\frac{z^2}{u^2-\rho_0^2}+\frac{\rho^2}{u^2}=1,\quad u\geq\rho_0;\quad -\frac{z^2}{\rho_0^2-v^2}+\frac{\rho^2}{v^2}=1,\quad v\leq\rho_0\ ,$$

where $2\rho_0$ is the focal distance and $\rho_0=(a^2-c^2)^{1/2}$. Now the surfaces of constant u and v are confocal oblate spheroids and confocal rotational hyperboloids, respectively. For small penetration and parallel field, the potential is[31]

$$\Phi=[-H_a\rho_0(u^2-\rho_0^2)^{1/2}-Af(u/\rho_0)](\rho_0^2-v^2)^{1/2}\ , \tag{30a}$$

whereas for perpendicular incidence,

$$\Phi=[-H_a-Af_1(u/\rho_0)]\frac{uv}{\rho_0}\cos\varphi\ , \tag{30b}$$

where

$$f(z)=1-(z^2-1)^{1/2}\arcsin(1/z)$$

and

$$f_1(z)=z\arcsin(1/z)-(z^2-1)^{1/2}/z$$

are functions related to associated Legendre functions of the second kind. In an analogous fashion to Sec. III A, the use of the boundary conditions at $u=a$, now $B_u=\mu H_u=0$, $J_{s,\varphi}=H_v$, and $J_{s,v}=-H_\varphi$, enables the derivation of the core shapes for small penetrations:

$$u'_{k,\parallel}(v',h_a)=1-\frac{h_a(1-e^{*2})^{1/2}}{2\pi e'[1-g_\parallel(e')]}\frac{|v'|}{1-v'^2}\ , \tag{31a}$$

$$u'_{k,\perp}(v',h_a)=1-\frac{h_a(1-e^{*2})^{1/2}}{2\pi e'[1-g_\perp(e')]}\times\frac{|e'^2(1-v'^2)-v'^2\cos^2\varphi|^{1/2}}{1-v'^2}\ , \tag{31b}$$

where $u'=u/a$ and $v'=v/a$ are normalized oblate coordinates ($-e^*\leq v'\leq e^*$) and

$$g_\parallel(e')=\frac{1+e'^2}{e'^3}(e'-\arctan e')\ ,$$

together with $g_\perp(e')=[1-g_\parallel(e')]/2$ are characteristic shape factors of the oblate spheroids.[30,31]

Moreover, using (31), we derive the initial magnetization for small fields, which coincides with (27), but with the actual $g_\beta(e')$ factors. In the limit $e'\to 0$ ($e^*\to 0$), $g_\parallel(0)=g_\perp(0)=\frac{1}{3}$ and (31) reduces to the result for spheres. Furthermore, for $e'\to\infty$ ($e^*\to 1$), $g_\parallel(\infty)=1$, $g_\perp(\infty)=0$, and $M'_\parallel$ diverges.

D. Oblate spheroids, numerical results

Using the numerical procedures of Sec. II B, we find the shielded volumes for arbitrary parallel applied fields $0\leq h_a\leq h_\parallel^*$ in oblate-spheroidal geometry. A variable polygonal line (r_j,θ_j) with N ranging from 21 to 33 is determined by minimizing $f_{\rm err}$. The shape changes of the core with h_a make it difficult to mesh the polygon, and so an equally spaced grid is used for small eccentricities. For greater eccentricities an adapted mesh with smaller intervals around $\theta=\pi/2$ is used.

In Figs. 8 and 9 are shown the shielded volumes for two different eccentricities. For $a/c=2$, $h_\parallel^*=3.960\,33$ (Fig. 8), the core's surface is onionlike and only at higher penetrations resembles the result for spheres. In the $\theta=\pi/2$ plane the field easily penetrates at lower fields, whereas at fields close to h^* penetration this becomes more difficult. The core's apex coincides with the pole in

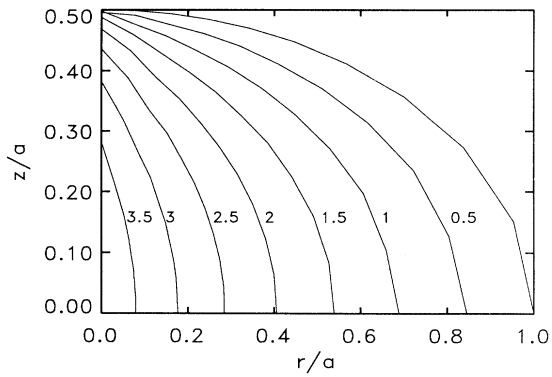

FIG. 8. Contours of the oblate spheroid and magnetically shielded cores when $a/c=2$ ($h_\parallel^*=3.960\,33$) at different applied fields $h=2\pi H/aJ_c$ (labels on the curves).

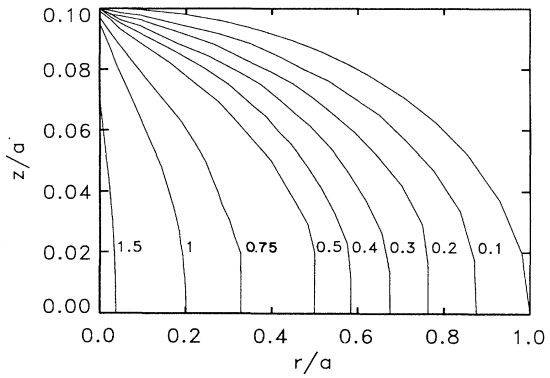

FIG. 9. First quadrant of the magnetically shielded volume for a prolate spheroid when $a/c=10$ ($h_{\parallel}^{*}=1.700\,68$). The same conventions are used as in Fig. 8.

a wider range of relative fields and goes deeply inside with a faster slope.

For a higher eccentricity $a/c=10$, $h_{\parallel}^{*}=1.700\,68$ (Fig. 9), the previous trends grow. The field easily penetrates in the $\theta=\pi/2$ plane, and the flux profile is highly nonlinear. In Fig. 9 the z-axis scale is expanded 5 times to match Fig. 8 and show that the field penetration is faster than for small eccentricities. At the $\theta=0$ line the behavior is opposite and the core's apex coincides with the pole for applied field up to $h_a \approx h^{*}/2$. For higher fields the core shows shapes more like those observed in spheres or prolate spheroids.

Using the derived shielding volume, we obtain the initial magnetization as well as hysteresis loops. Integral procedures similar to those of (20)–(22) were used. In Figs. 10 and 11 are collected those results for applied fields $h^{*}/4$, $h^{*}/2$, and h^{*}. For both eccentricities the magnetization at saturation takes the same values, but is

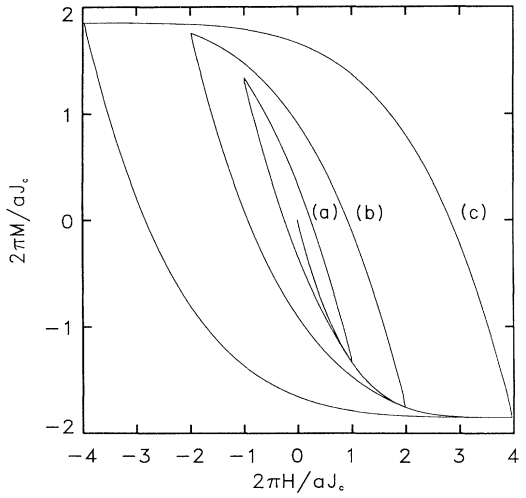

FIG. 10. Initial magnetizations $M_{\parallel}$ and hysteresis loops for an oblate spheroid with $a/c=2$ ($h_{\parallel}^{*}=3.960\,33$) for (a) $h_{\max}=h_{\parallel}^{*}/4$, (b) $h_{\parallel}^{*}/2$, and (c) $h_{\parallel}^{*}$.

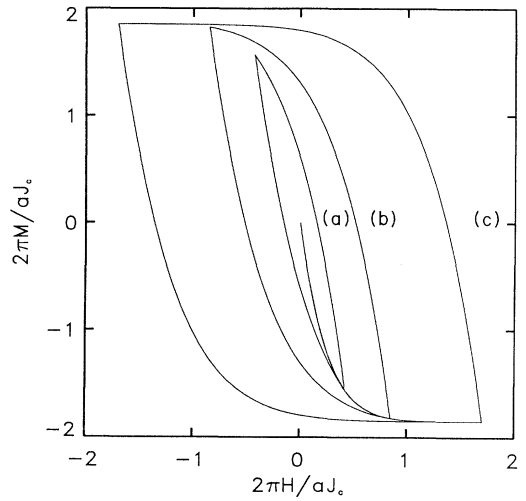

FIG. 11. Initial magnetizations $M_{\parallel}$ and hysteresis loops for an oblate spheroid when $a/c=10$ ($h_{\parallel}^{*}=1.700\,68$) for (a) $h_{\max}=h_{\parallel}^{*}/4$, (b) $h_{\parallel}^{*}/2$, and (c) $h_{\parallel}^{*}$.

reached for smaller fields when the eccentricity increases, which implies a steeper slope of the initial M-H curve.

IV. DISCUSSION OF THE BLM RESULTS

As many experimental results have been analyzed with the predictions of BLM for slabs and cylinders, it is useful to compare these results with the initial magnetizations obtained here. To this end, in Fig. 12 we show M/H^{*} vs H/H^{*} for those geometries.

For slabs it is well known, when the field is parallel to the surface,[4] that the initial magnetization for $H_a \leq H_{\parallel}^{*}$ is

$$\frac{M_{\parallel}}{H_{\parallel}^{*}}=\frac{1}{2}\left[\frac{H_a}{H_{\parallel}^{*}}\right]^2-\frac{H_a}{H_{\parallel}^{*}}\ ,$$

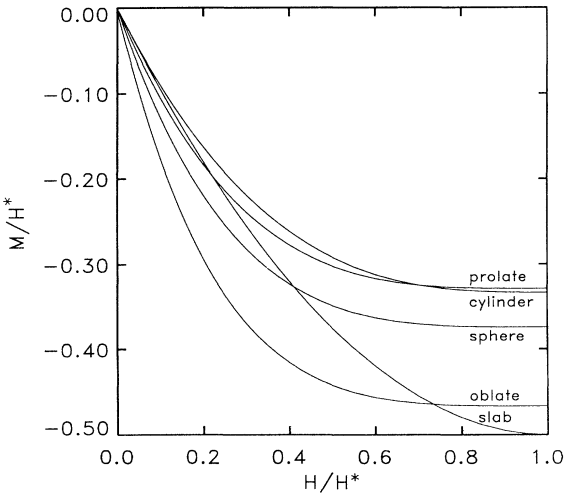

FIG. 12. Comparisons of the initial magnetization for slabs, cylinders, spheres, and spheroids (with $a/c=2$) in dimensionless units.

where $H_{\parallel}^{*}=J_c d/2$ and d is the slab width.

For cylinders with the field $H_a \leq H_{\parallel}^{*}$ parallel to the axis,[4]

$$\frac{M_{\parallel}}{H_{\parallel}^{*}}=\left[\frac{H_a}{H_{\parallel}^{*}}\right]^2-\frac{H_a}{H_{\parallel}^{*}}-\frac{1}{3}\left[\frac{H_a}{H_{\parallel}^{*}}\right]^3,$$

where now $H_{\parallel}^{*}=J_c a$, with a being the cylinder radius.

There are no analytical solutions[19–24] for perpendicular field except in the two limits. For full penetration, $H_{\perp}^{*}=2J_c a/\pi$,[19] and the maximum value of the magnetization is $M_{\perp}/H_{\perp}^{*}=-\frac{2}{3}$.[20] For small penetration, $M_{\perp}/H_{\perp}^{*}=-2H_a/H_{\perp}^{*}$. Zenkevich, Zheltov, and Romanyuk[224] and Pang, Campbell, and McLaren[23] give simple approximate formulas for $M_{\perp}/H_{\perp}^{*}$. We use in this discussion the results of Pang, Campbell, and McLaren,[23] which are not exact, but for $H_a<H_{\perp}^{*}$ are claimed to follow the numerical results within 10%:

$$\frac{M_{\perp}}{H_{\perp}^{*}}=2\left[\frac{H_a}{H_{\perp}^{*}}\right]^2-2\frac{H_a}{H_{\perp}^{*}}-\frac{2}{3}\left[\frac{H_a}{H_{\perp}^{*}}\right]^3.$$

The slope at the origin of $M_{\parallel}/H_{\parallel}^{*}$ for cylinders and slabs is -1. This should be compared with the result $1/(1-g_{\beta})$ for spheres and spheroids, following (27). For prolate spheroids and small fields, both $M_{\parallel}$ and $M_{\perp}$ change continuously with the eccentricity from the value for spheres $\frac{3}{2}$ [$g_{\beta}(0)=\frac{1}{3}$] to that for cylinders [$g_{\parallel}(1)=0$, $g_{\perp}/(1)=\frac{1}{2}$]. This is due to the continuity for the core (26) which changes between those limits giving for spheres the expression (6) and

$$r'_{k,\perp}=1-3h_a/4\pi(1-\cos^2\varphi\sin^2\theta)^{1/2},$$

and giving for cylinders, $\rho_{k,\parallel}=a(1-H_a/J_c a)$ and $\rho_{k,\perp}=a(1-2H_a/J_c a\sin\varphi)$.

Moreover, for oblate spheroids $M_{\perp}$ changes with eccentricity from the result for spheres to that for slabs [$g_{\parallel}(\infty)=1$, $g_{\perp}(\infty)=0$]. With the usual definition of relative directions, $M_{\perp}$ in oblate spheroids has the limit $M_{\parallel}$ in slabs.

It should be noted that the M/H slopes for the Meissner state are the same as (27). Then there is no discontinuity when H_a reaches the superheating field value $H_{\rm sh}=H_{c1}[1-g_{\beta}(e)]$ and the flux starts to penetrate. Only at higher fields would deviations from linearity be observed.

The values of the magnetization at saturation $H_a/H^{*}\rightarrow 1$) are $M_{\parallel}/H_{\parallel}^{*}=-\frac{1}{2}$ for slabs, $-\frac{1}{3}$ for cylinders, and $-\frac{3}{8}$ for spheres (10). Note that the sphere value is intermediate between cylinders and slabs. However, the value of $M_{\perp}/H_{\perp}^{*}$ for spheres is higher than for cylinders.

For any field the absolute value of $M_{\parallel}/H_{\parallel}^{*}$ for spheres is always higher than the corresponding one for cylinders, but it crosses the predictions for slabs. A similar behavior is observed for prolate spheroids when $a/b=2$. The slope at the origin -1.210 is lower than that for cylinders, but before saturation $M_{\parallel}$ crosses over the values corresponding to cylinders. For $a/b=10$ the slope at the origin is already -1.021 and the difference with the result for cylinders is negligible. However, at saturation the slope almost reaches the limiting value $M_{\parallel}/H_{\parallel}^{*}==2\pi/32$.

For oblate spheroids the results again show continuity with the behavior of spheres. Moreover, for $a/c=2$ the slope at the origin is -2.115 and $M_{\parallel}$ is always lower. In the scale of Fig. 12, $M_{\parallel}/H_{\parallel}^{*}$ diverges as $H_{\parallel}^{*}$ goes to zero with increasing e^{*} (already for $a/c=10$ the slope is 7.179).

From the above comparisons it can be concluded that for elongated shapes the use of the BLM solutions for cylinders may give an appropriate description of the initial flux profile and its related properties, whereas at saturation there are differences, although small.

Furthermore, for flat shapes our results prove that the approximation of slabs may be used to describe the characteristics only at small penetration and when the field is parallel to the surface. For perpendicular incidence shape effects become very important because the field easily penetrates in the equatorial plane, whereas it hardly does so at the poles. This greatly affects the magnetization, which shows steeper slopes than in other geometries. This behavior has no analog in the previous results for slabs and cylinders and discloses the failure of these geometries to capture the magnetic characteristics of platelike geometries.

It is worthwhile to remember at this point the platelike shapes observed in most HTS granular material. Certainly, for oriented materials, when the field is parallel to the crystallographic c axis, the above results indicate the inability of slab or cylinder results to match the main characteristics of the grain-flux profile. In this case the above analysis using oblate spheroids gives a more appropriate description.

Previous studies on classic type-II superconductors[28,32] and HTS (Refs. 33 and 34) disks in a transverse field show many of the characteristics derived for oblate spheroids when the field is parallel to its axis. Some of the conclusions of such studies that nicely match our theoretical results are the following: (i) Small fields easily penetrate at the edge of the disks, but attempts to fit the experimental data within critical-state models[28] using a planar set of current loops need an azimuthal component of the current density throughout the surface. (ii) The critical field is reached at the faces of the disks, and the flux trapped (or shielded) in the center depends more on the thickness than on the disk radius. (iii) As the flux penetrates, the slope of M vs H decreases.

Although the results derived for oblate spheroids will be accurate enough for very flat disks, the methods developed here may be implemented for finite-cylinder geometries. For external fields parallel to the axis, the system also has rotational symmetry, but now the field inside the cylinder is not parallel to the axis (i.e., both H_z and H_{ρ} exist) and the field in the neighborhood of the cylinder must show octopolar and higher-order odd-multipolar terms in addition to the dipolar terms.

V. CONCLUSIONS

The penetration of magnetic flux in HTS ceramics and powders has been modeled with three-dimensional BLM

solutions.[3,4] As the model assumes strong pinning and fields $H > H_{c1}$, the validity of the derived expressions extends to the irreversibility line.[35]

To achieve this we analyzed in a self-consistent way three finite geometries of the grains: spheres, prolate spheroids, and oblate spheroids within critical-state models.

For spheres we reproduced and completed the few analytical results[20] obtained in the limits of small and full penetration. Moreover, we implemented numerical procedures which allow the determination of the full-penetration range, as well as the derivation of the initial magnetization and hysteresis loops.

For both prolate and oblate spheroids, we derived analytic results in the small-penetration limit for both parallel and perpendicular fields. In addition, for parallel fields we derived the magnetization at saturation and developed numerical procedures for the full-penetration range. In each case we found the flux penetration, initial magnetization, and hysteresis loops for two eccentricities corresponding to aspect ratios of 2 and 10.

Further, we compared these results mutually and with the analytic results for slabs and cylinders. The main conclusions are the following.

(i) Flux penetration in spheres and spheroids is nonlinear with the penetration depth and depends on the azimuth angle. In prolate spheroids the nonlinearity in the equatorial plane decreases with eccentricity, whereas for oblate spheroids it increases.

(ii) The slope at the origin of the initial magnetization $M_{\parallel}$ for spheres is steeper than for slabs and cylinders. For prolate spheroids a smooth variation of the behavior with the eccentricity interpolates between the results of spheres and cylinders for both parallel and perpendicular fields. For oblate spheroids and perpendicular incidence there is a continuous variation from spheres to slabs, but for parallel fields a new and different behavior was found.

(iii) The value of $M_{\parallel}/H_{\parallel}^{*}$ at saturation for spheres is intermediate between those for slabs and cylinders and is lower than $M_{\perp}/H_{\perp}^{*}$ for cylinders. In the case of prolate spheroids, $M_{\parallel}/H_{\parallel}^{*}$ changes from the value for spheres to a slightly higher value than for cylinders. $M_{\parallel}/H_{\parallel}^{*}$ in oblate spheroids is not bounded at higher eccentricity.

The nonlinearity in the flux profile as well as the characteristics found for parallel incidence in oblate spheroids reveal the inability of other simple geometries to mimic the properties of platelike HTS grains.

Our results provide a more coherent basis for the analysis of the experimental results on superconducting disks.[28,32–34] It also may allow a better understanding of HTS single-crystal properties.[26]

ACKNOWLEDGMENTS

This research has been supported in part by the Spanish projects C.I.C.Y.T. (No. MAT90-0362) and MIDAS (No. 89/3797). Moreover, R. Navarro wishes to acknowledge support from D.G.I.C.Y.T. Grant No. BE91-071.

*Permanent address: Instituto de Ciencia de Materiales de Aragon, C.S.I.C.-U of Zaragoza, 50009 Zaragoza, Spain.

[1]R. Navarro and L. J. Campbell (unpublished).
[2]M. L. Hodgdon, R. Navarro, and L. J. Campbell, Europhys. Lett. (to be published).
[3]H. London, Phys. Lett. **6**, 162 (1963).
[4]C. P. Bean, Phys. Rev. Lett. **8**, 250 (1962); Rev. Mod. Phys. **36**, 31 (1964).
[5]Y. B. Kim, C. F. Hempstead, and A. J. Strnad, Phys. Rev. Lett. **9**, 306 (1962); Phys. Rev. **129**, 528 (1963).
[6]G. Ravi Kumar and P. Chaddah, Phys. Rev. B **39**, 4704 (1989).
[7]P. Chaddah, G. Ravi Kumar, A. K. Grover, C. Radhakrishnamurty, and G. U. Subba Rao, Cryogenics **29**, 907 (1989).
[8]H. Dersch and G. Blatter, Phys. Rev. B **38** 11 391 (1988).
[9]M. Xu, D. Shi, and R. F. Fox, Phys. Rev. B **42**, 10 773 (1990).
[10]D.-X. Chen and R. B. Goldfarb, J. Appl. Phys. **66**, 2489 (1989).
[11]D.-X. Chen, A. Sanchez, and J. S. Muñoz, J. Appl. Phys. **67**, 3430 (1990).
[12]D.-X. Chen, A. Sanchez, J. Nogues, and J. S. Muñoz, Phys. Rev. B **41**, 9510 (1990).
[13]E. M. Gyorgy, R. B. van Dover, K. A. Jackson, L. F. Schneemeyer, and J. V. Waszczak, Appl. Phys. Lett. **55**, 283 (1989).
[14]D.-X. Chen, J. Nogues, and K. V. Rao, Cryogenics **29**, 800 (1989).
[15]T. Matsushita, E. S. Otabe, T. Matsuno, M. Murakami, and K. Kitazawa, Physica C **170**, 375 (1990).
[16]R. Navarro, F. Lera, A. Badia, C. Rillo, J. Bartolome, W. L. Lechter, and L. E. Toth (unpublished).
[17]R. L. Peterson, Phys. Rev. B **40**, 2678 (1989).
[18]L. Krusin-Elbaum, A. P. Malozemoff, D. C. Cronemeyer, F. Holtzberg, J. R. Clem, and Z. Hao, J. App. Phys. **67**, 4670 (1990).
[19]W. J. Carr, Jr., Phys. Rev. B **11**, 1547 (1975); J. Appl. Phys. **46**, 4043 (1975); *ac Loss and Macroscopic Theory of Superconductors* (Gordon and Breach, New York, 1983).
[20]A. M. Campbell and J. E. Evetts, Adv. Phys. **21**, 199 (1972).
[21]Y. Kato, M. Hanawaka, and K. Yamafuji, Jpn. J. Appl. Phys. **15**, 695 (1976).
[22]M. Ashkin, J. Appl. Phys. **50**, 7060 (1979).
[23]C. Y. Pang, A. M. Campbell, and P. G. McLaren, IEEE Trans. Magn. **MAG-17**, 134 (1981).
[24]V. B. Zenkevich, V. V. Zheltov, and A. S. Romanyuk, Dokl. Akad. Nauk SSSR **250**, 339 (1980) [Sov. Phys. Dokl. **25**, 210 (1980)].
[25]K. V. Bhagwat and P. Chaddah, Physica C **166**, 1 (1990).
[26]V. M. Krasnov, V. A. Larkin, and V. V. Ryazanov, Physica C **174**, 440 (1991).
[27]J. R. Clem, Physica C **153-155**, 50 (1988).
[28]D. J. Frankel, J. Appl. Phys. **50**, 5402 (1979).
[29]J. R. Clem, J. Appl. Phys. **50**, 3518 (1979).
[30]See, for example, J. Van Bladel, *Electromagnetic Fields* (Hemisphere, Washington, 1985).

[31]F. Ollendörf, *Technische Elektrodynamik* (Springer-Verlag, Wien, 1952).
[32]M. N. Kunchur and S. J. Poon, Phys. Rev. B **43**, 2916 (1991).
[33]M. A.-K. Mohamed, J. Jung, and J. P. Franck, Phys. Rev. B **39**, 9614 (1989).
[34]M. Däumlling and D. C. Larbalestier, Phys. Rev B **40**, 9350 (1989).
[35]Youwen Xu and M. Suenaga, Phys. Rev. B **43**, 5516 (1991).